ACS APPLIED MATERIALS & INTERFACES

www.acsami.org Research Article

Nonvolatile Electric Control of Exciton Complexes in Monolayer $MoSe_2$ with Two-Dimensional Ferroelectric $CuInP_2S_6$

Xiaoyu Mao, Jun Fu, Chen Chen, Yue Li, Heng Liu, Ming Gong,* and Hualing Zeng*

Cite This: *ACS Appl. Mater. Interfaces* 2021, 13, 24250−24257 Read Online

ACCESS | Metrics & More | Article Recommendations | SI Supporting Information

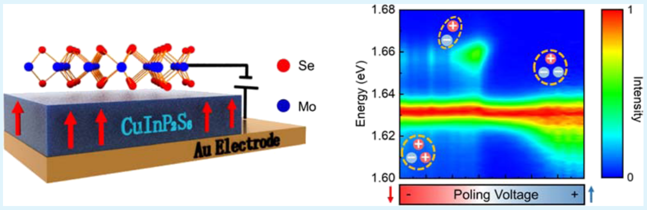

ABSTRACT: Monolayer transition-metal dichalcogenides (TMDs) have provided a platform to investigate the excitonic states at the two-dimensional (2D) limit. The inherent properties of excitons in TMDs, such as the photoluminescence quantum yield, the charge states, and even the binding energy, can be effectively controlled via electrostatic gating, selective carrier doping, or substrate dielectric engineering. Here, aiming for the nonvolatile electrical tunability of excitonic states and thereby the optical property of TMDs, we demonstrate a 2D ferroelectric heterostructure with monolayer $MoSe_2$ and ultrathin $CuInP_2S_6$ (CIPS). In the heterostructure, the electric polarization of CIPS results in continuous, global, and large electronic modulation in monolayer $MoSe_2$. With the saturated ferroelectric polarization of CIPS, electron-doped or hole-doped $MoSe_2$ is realized in a single device. The carrier density tunability in the heterostructure is as high as 5×10^{12} cm^{-2}. The nonvolatile behavior of these devices up to 3 months is also characterized. Our results provide a new and practical strategy for low-power consumption and agelong tunable optoelectronic devices.

KEYWORDS: *exciton, $MoSe_2$, $CuInP_2S_6$, ferroelectricity, 2D ferroelectric heterostructure*

INTRODUCTION

Monolayer transition-metal dichalcogenides (TMDs) have attracted extensive investigations on band structure engineering,[1−3] strong interactions between the electron and holes,[4−8] and the valley degree of freedom.[9−11] Among the advancements achieved, tuning the electronic structure is one of the most attractive issues due to their nature as a new class of two-dimensional (2D) direct band gap semiconductors.[12−15] In general, it can be realized either through chemical doping or applying the electrostatic field effect with conventional dielectrics. For example, selectively introducing defects or dopants in monolayer TMDs leads to the formation of a p−n junction.[16−18] Incorporating the field-effect transistor (FET) device, n-type or p-type monolayer TMDs are realized via electrical gating.[19−21] However, the chemical method inevitably brings the disorder effect which enhances the carrier scattering and thereby leads to the decreased conductivity and spectral broadening in TMDs, while the FET structure requires application of the gate voltage to maintain the doping which fails to meet the standard of a low-power consumption device. A disorder-free and nonvolatile scheme is anticipated to overcome the challenges.

Very recently, some new ways based on bulk perovskite ferroelectrics, including lead zirconate titanate (PZT), P(VDF-TrFE), and lithium niobite, have been utilized to modulate the light emission in 2D TMDs.[22−28] In these systems, the emission of TMDs can be controlled by the predefined ferroelectric domains with opposite polarizations, which were achieved through strain engineering and tip-enhanced local electric field. Even so, as the key step for device applications, the continuous and global ferroelectric tuning of emission in TMDs has not yet been reported. One underlying origin is the high poling voltage required in conventional ferroelectrics because of their nature as large band gap insulators with a relatively large film thickness.[29] Moreover, for oxide perovskite ferroelectrics, the perfect Coulomb screening of electric polarization at the interface relies on rigorous lattice matching, which is difficult to realize when coupling with monolayer TMDs.[30,31] As a result, the ferroelectric modulation ability is limited in this type of quasi-2D heterostructures.

Here, to resolve the above problems, we demonstrate the nonvolatile electric doping effect by constructing a device based on monolayer $MoSe_2$ and 2D ferroelectric $CuInP_2S_6$ (CIPS). In this device, a retentive electrostatic field is introduced from the ferroelectric layer without direct coupling between the sample and the dielectric substrate. The device is fabricated via the mechanical stacking method, showing that the spontaneous polarization of CIPS can provide a strong positive and negative electric field, which can induce

Received: February 16, 2021
Accepted: April 28, 2021
Published: May 11, 2021

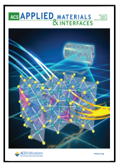

https://doi.org/10.1021/acsami.1c03067
ACS Appl. Mater. Interfaces 2021, 13, 24250−24257

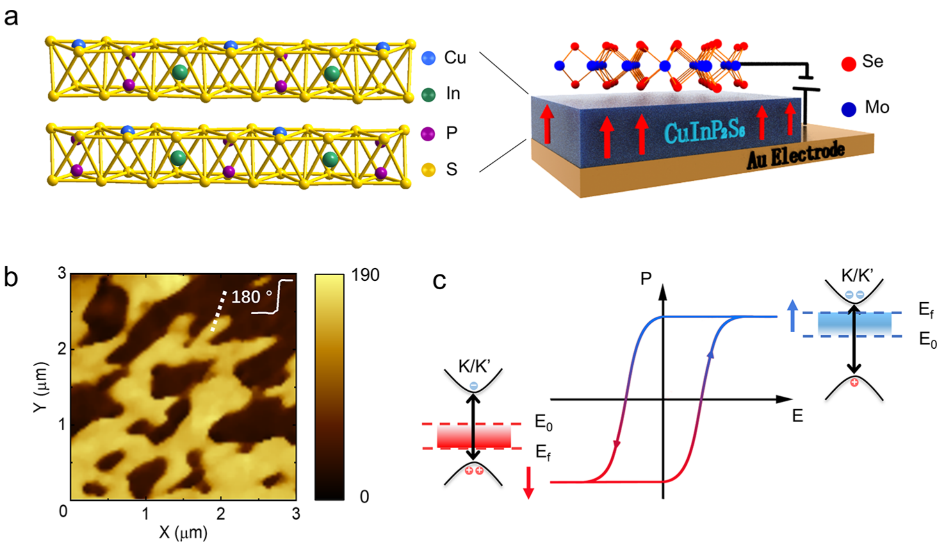

Figure 1. Device concept of 2D ferroelectric doping. (a) 3D schematic diagram of the ferroelectric heterostructure. The red arrows indicate the ferroelectric polarization. The zoomed area shows the crystal structure of ferroelectric CIPS. (b) PFM phase of CIPS flakes in the OOP direction; the inset shows the PFM phase along the white arrow. (c) Ferroelectric hysteresis loop and the band energy of $MoSe_2$ at the corresponding polarization state. The blue and red arrows indicate the polarization directions of CIPS. The up (down) polarization state of CIPS provides negative (positive) screening charges for $MoSe_2$, which induces n (p)-type doping. The Fermi energy shift is shown in the diagram.

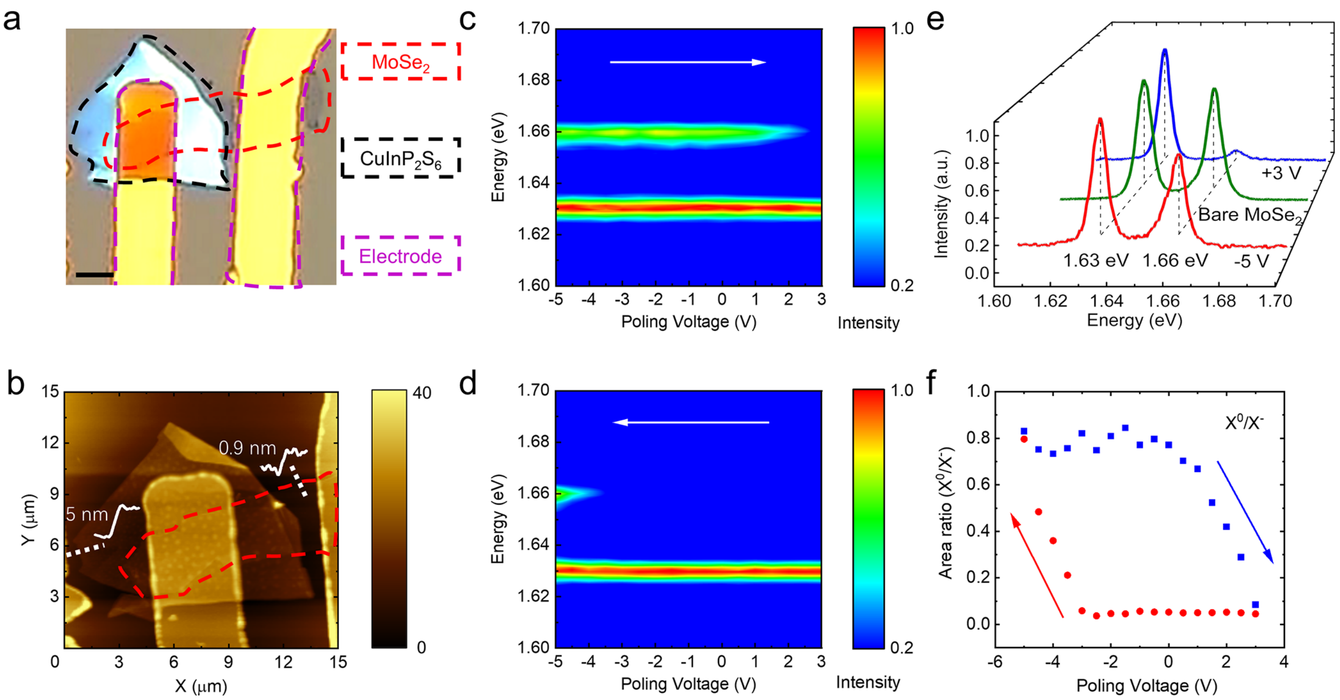

Figure 2. Nonvolatile electric modulation on excitonic states. (a) Optical image and (b) AFM topography of Device 1#. Monolayer $MoSe_2$, few-layer CIPS, and electrodes are indicated by red, black, and purple dashed frames, respectively. The thinnest area of CIPS in the device is 5 nm. The thickness for monolayer $MoSe_2$ is determined to be 0.9 nm. The scale bar is 3 μm. (c) PL spectra of $MoSe_2$ as the pulsed polarization voltage changes from −5 to +3 V and (d) backward at 7 K. (e) PL spectrum of bare monolayer $MoSe_2$ (green line) and device 1# after −5 V (red line) and +3 V (blue line) pulsed polarization at 7 K. (f) The PL intensity ratio of (X^0/X^-) depends on the pulsed polarization voltage variation.

controllable excitonic states between n-type and p-type emissions from the photoluminescence (PL) spectra. High quality of the emission spectra is also demonstrated after 3 months. We have also studied the physics of exciton and trion PL peaks at low temperature to a high doping level, in which the long tail from the three-body recoil effect is observed. The doping capability of the device is estimated to be as high as over 5×10^{12} cm^{-2}. Our results provide a new strategy for developing practical 2D ferroelectric heterostructure-based optoelectronics.

RESULTS AND DISCUSSION

The 2D ferroelectric device is depicted in Figure 1a, in which the CIPS ultrathin flake is sandwiched by the top monolayer $MoSe_2$ and the bottom Au electrode. In CIPS, the sulfur atoms are covalently interconnected to form a frame and the Cu, In,

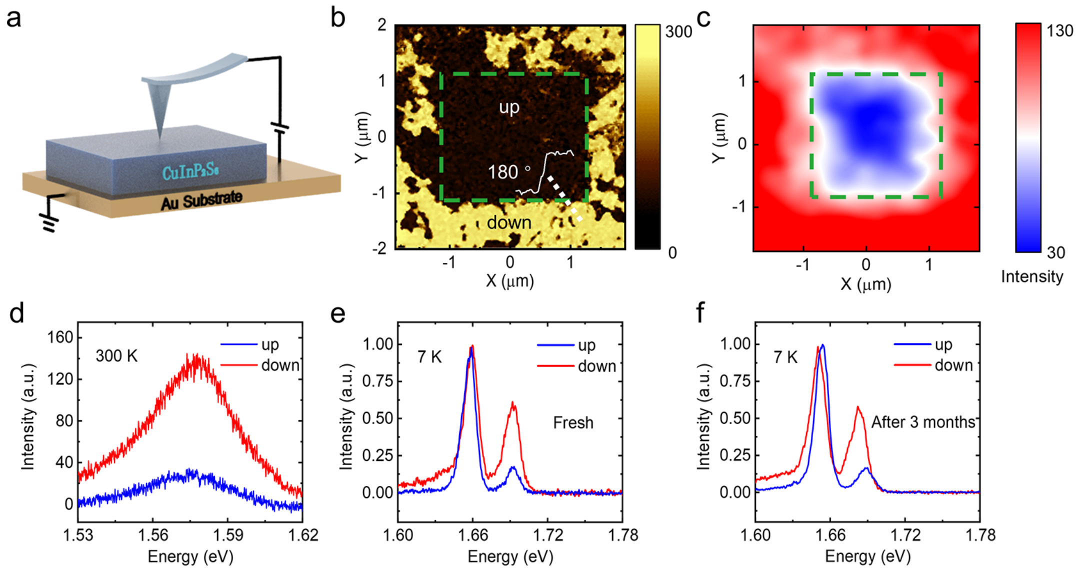

Figure 3. Ferroelectric domain imaging by PL mapping and nonvolatility of ferroelectric CIPS. (a) 3D schematic diagram of the experiment configuration for ferroelectric domain writing. (b) PFM phase image of CIPS with opposite polarization (upward in the box and downward outside the box) written by the PFM tip. (c) Integral PL intensity mapping of $MoSe_2$ in the same region at 300 K. The low-intensity square corresponds to the upward polarization region of CIPS. (d) PL spectra of upward (blue line) and downward (red line) areas at 300 and (e) 7 K right after PFM writing. (f) PL spectra of upward (blue line) and downward (red line) areas at 7 K 3 months after PFM writing.

and P−P pair atoms fill in the sulfur cages with a triangular pattern, respectively. The out-of-plane (OOP) ferroelectricity of CIPS originates from the Cu ion skewing off the inversion symmetry center in each single layer. The polarization in CIPS can be controlled by the bias across the sample. When the bias is applied, the upper and lower surfaces may accumulate opposite charges, which can then influence the carrier doping in monolayer $MoSe_2$. This equivalently induces carrier doping in monolayer $MoSe_2$ from the screening effect.

First, we confirm the ferroelectricity of CIPS by performing the piezoresponse force microscopy (PFM) test on CIPS thin flakes (~30 nm) at ambient conditions (see Figure 1b). The phase contrast of 180° between the adjacent domains indicates the antiparallel alignment of the OOP electric polarizations. Moreover, by comparing the atomic force microscopy (AFM) measurement and the PFM amplitude image of the same area (see Figure S1), no obvious correlation between the ferroelectric domain structures and the morphologies is observed, indicative of clear ferroelectric CIPS.[32] According to the sample thickness and polarization flipping voltage (see Figure S1), the coercive field of CIPS is about 670 kV/cm.

Next, we show the mechanism of 2D ferroelectric doping in our device. In Figure 1a, the top $MoSe_2$ and the bottom Au electrode not only function as an electric polarization switch but also serve as the Coulomb screening layers. The induced screening charges by the electric polarization in CIPS result in the shift of the Fermi energy level in $MoSe_2$. Consequently, the excitonic optical transitions at K/K′ valleys in monolayer $MoSe_2$ are strongly affected. With this mechanism (see Figure 1c), n-type or p-type doping in $MoSe_2$ can be realized by controlling the direction of the electric polarization in CIPS to be upward or downward, respectively. Furthermore, from the ferroelectric hysteresis of CIPS (see Figure S1), this type of electronic doping is nonvolatile.

We have prepared and studied 25 ferroelectric devices in total, all of which show similar behaviors. The device fabrication process is detailed in the Methods section. Figure 2 presents the results from a typical device (termed as Device 1#). This sample has a thickness of about 5 nm, as evidenced from AFM topography (Figure 2b). This thickness is slightly greater than the thickness of 4 nm required for switchable polarization in CIPS reported in ref 28; thus, the reversible ferroelectric doping in our device is feasible. We measured the PL spectrum from $MoSe_2$ under 7 K. This spectrum depends strongly on the electric polarization in CIPS, although during the PL measurement, the voltage is removed. In Figure 2c,d, we present the PL spectrum by scanning the voltage from −5 to +3 V and backward, respectively, which yield different behaviors due to the electric hysteresis effect of CIPS. Importantly, the peak positions in these conditions are the same as those with bare monolayer $MoSe_2$ (see Figure 2e, with an exciton X^0 peak at 1.66 eV and trion $X^{\pm}$ at 1.63 eV). No obvious broadening of the spectrum is observed for the three cases in Figure 2e; thus, CIPS only plays the role of carrier doping. In Figure 2f, we report the electric hysteresis effect from the intensity ratio (X^0/X^-) of the PL spectra, which shows a perfect hysteresis curve (see Figure 2f). Since this is a room-temperature ferroelectric (with critical temperature $T_c \sim$ 320 K), a similar curve can be observed even under ambient conditions (see Figure S2). Figure S3 shows the results of the same experiments performed by replacing CIPS with SiO_2, which is a non-ferroelectric material. No such hysteresis curve was observed, showing that the emission is indeed controlled by the electric hysteresis effect of CIPS.

Figure 2f is not the most transparent manifestation of the nonvolatile effect. To this end, in Figure 3, we study the relationship between the electric polarization and PL spectrum through domain writing in Device 3# via the PFM tip (see the structure in Figure 3a and the Methods section), which can induce the flip of polarization by a local electric field in a square region (2 μm × 2 μm). Figure 3b displays the phase image of the artificially created ferroelectric domain structure at room temperature, in which the contrast of 180° indicates the antiparallel polarization directions of the two adjacent

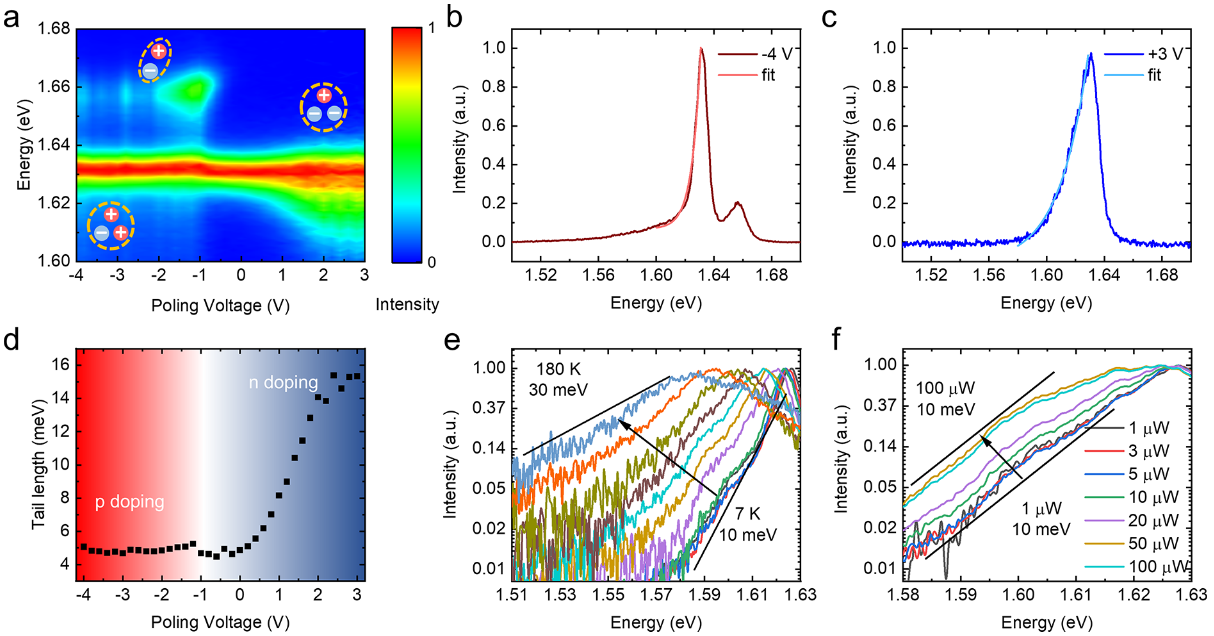

Figure 4. Three-body carrier recoil effect in charged excitonic optical transitions. (a) $MoSe_2$ PL spectrum as the poling voltage changes from −4 to +3 V. The exciton species are represented by hydrogen and hydrogen-ion-like models shown. (b) Asymmetric PL spectra of $MoSe_2$ at +3 and (c) −4 V poling. The pink line in (b) and the light blue line in (c) show the exponential fitting of the low-energy tail of trion peaks. (d) Fitted tail length of the trion peak as a function of the poling voltage. (e) Temperature dependence of the trion tail from 7 to 180 K at +3 V. (f) Relationship of the trion tail and laser power at 7 K with a +3 V poling voltage.

domains. After that, we immediately measured the PL mapping in the same region, which is given in Figure 3c, showing that the two regions with antiparallel polarizations exhibit totally different spectra. At room temperature, a broad peak is observed (see Figure 3d); however, at low temperature, the two peaks (X^0 and X^-) can be clearly distinguished in these two regimes (see Figure 3e). This electric polarization can persist for an extraordinary time. In Figure 3f, we present the results of the same experiments for the same sample after 3 months, which yields almost the same PL spectrum. This result demonstrates the nonvolatile electric controllability of the exciton state in monolayer $MoSe_2$ by 2D CIPS.

In addition to the featured nonvolatility, we demonstrate the remarkable gating efficiency of our heterostructure device. With the same ferroelectric device structure, the electrical polarization method is changed from the pulse mode to the continuous-voltage mode (or the DC voltage mode). Figure 4a shows the PL mapping from Device 4# by changing the DC voltage from −4 to 3 V at 7 K. Differing from the results from Device 1#, except for the X^0 PL peak, the photon emissions from X^+ and X^- states can be distinguished. For hole and electron trions in monolayer $MoSe_2$, due to the same binding energy and similar effective mass values, there are no observable spectroscopic differences such as the peak position or lineshape in the PL spectrum. Here, the assignment of the PL peaks to X^+ and X^- is based on the doping process of the ferroelectric device as discussed and verified previously. In the PL mapping, clear X^0 emissions are observed within the DC voltage ranging from −2 to −1 V. Therefore, below −2 V or above −1 V electric poling in the device, different types of doping from the CIPS thin layer lead to the formation of X^+ or X^-, respectively. The observation of hole trions in monolayer $MoSe_2$ under a negative poling voltage indicates the change of its electronic structure from n-type to p-type, which suggests the ultra-high electrostatic doping efficiency of our device if compared with that of the conventional oxide dielectrics-based gating method. The remarkable gating ability is attributed to the saturated electric polarizations of CIPS under continuous voltage polarizing. To further confirm the n-type or p-type doping in monolayer $MoSe_2$ by the electric polarization of CIPS, we fabricated a CIPS/$MoSe_2$ FET and observed a similar doping behavior, as shown in Figure S5.

This setup enables us to observe the asymmetry of the X^+/X^- spectra away from the Lorentz lineshape, probably from the absence of disorder during charge doping. As shown in Figure 4b,c, under −4 and +3 V poling, both the X^+ and X^- PL peaks are asymmetric with long tails at the low-energy side. The observed broad lineshapes are due to the charge recoil effect stemming from the three-particle nature of trions. Unlike the radiative recombination of neutral excitons, which occurs only at the Brillouin zone center, excited trions can radiatively decay with a non-zero momentum by kicking out an electron or hole. The schematic for the charge recoil effect is shown in Figure S4. With the energy and momentum conservation, the emitted photon energy from the recombination of trions is given by $\hbar\omega_T = E^0_{\text{trion}} - \frac{M_X}{M_e}E_{KE}$, where E^0_{trion} is the zero-momentum trion energy, M_X is the exciton mass, M_e is the effective electron (hole) mass, and E_{KE} is the electron (hole) kinetic energy. We fitted the low-energy PL tail with an exponential function and extracted the tail length as a function of the DC poling voltage, as shown in Figure 4d.[33] The dependence of the tail length with the DC bias originates from the shift of E_F and the thermal excitation of charge carriers. For the latter contribution, it follows the Boltzmann distribution. Therefore, by fixing the E_F with a DC poling voltage of +3 V, we found that the tail length of the X^- PL peak increased from 10 to 30 meV as the temperature changed from 7 to 180 K (Figure 4e). We also performed an excitation power dependence study at DC +3 V poling in Figure 4f. The tail length is almost the same

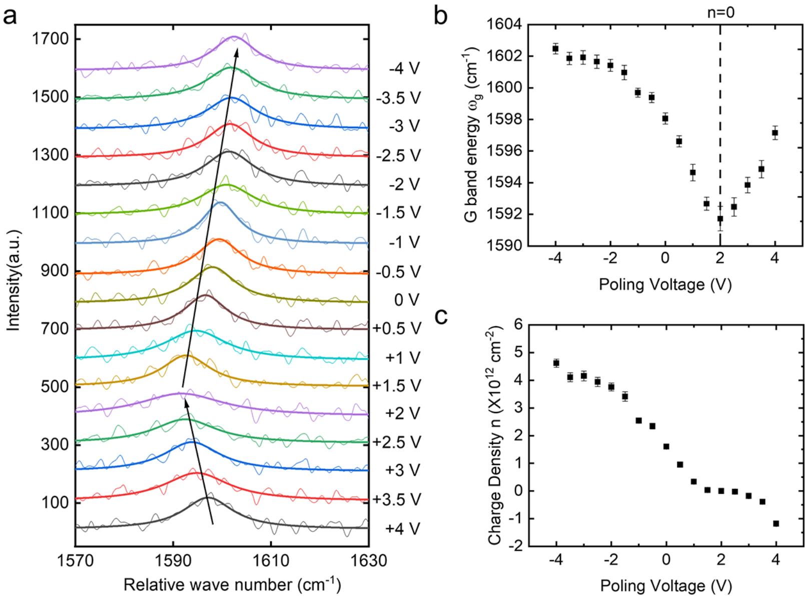

Figure 5. Quantification of the charge doping density benchmarked by the graphene−CIPS layer hybrid structure. (a) G mode Raman spectrum as the poling voltage varies from +4 to −4 V at 7 K. (b) The extracted G mode energy ω_g varies with the poling voltage. The dashed line indicates the neutral point for graphene. (c) The converted charge density in graphene changes with the poling voltage.

as the laser power varies from 1 to 100 μW. This characteristic behavior, which is independent of the laser power but relies on temperature, helps us to exclude the origin of the observed long low-energy tail from the PL spectrum of defects and the many-body collision.

Then, it is natural to ask how many electrons or holes can be doped in this type of 2D ferroelectric heterostructure. In the device, the doped carriers are realized from the screening effect, which is the same as the carrier density at the surface of CIPS. To perform an accurate estimation of the doping capability for ferroelectric CIPS, the screening effect in the 2D ferroelectric heterostructure should be maximized. For graphene, its semi-metallic nature certainly provides a better screen effect for the CIPS surface charges than that for semiconducting monolayer MoSe$_2$. For this reason, we replace MoSe$_2$ with single-layer graphene. This platform has the advantage that the Fermi energy is directly given by $E_F = -\text{sgn}(n)\hbar\nu_F\sqrt{(\pi|n|)}$, where ν_F ($\sim10^6$ m/s) is the Fermi velocity and n is the surface charge density. Therefore, the probe on the E_F of graphene allows the estimation of the charge density n, whose amount is equal to the induced carrier doping density in the ferroelectric device. The E_F of graphene can be measured through the Raman spectrum as the change in the doping level results in stiffening or softening of the G band phonons.[34−36] As shown in Figure 5a, the G mode peak shifts with the varying poling voltages at 7 K. We summarized the G mode frequency ω_g as a function of the poling voltage (Figure 5b), from which we conclude that $n = 0$ under a +2 V voltage modulation. According to previous study, the carrier density n of graphene follows ω_g according to

$$\omega_g = \omega_g^0 + \lambda\hbar\nu_F\sqrt{\pi|n|}$$

where $\lambda = 0.047$ from our best fitting. The correspondence between the charge density n and poling voltage is shown in Figure 5c. We found that the ferroelectric CIPS layer can induce a carrier doping density as high as 5×10^{12} cm^{-2} in the heterostructure device, from which we estimate the change in the Fermi energy E_F at about 0.38 eV. This carrier density doping is comparable with that obtained using the conventional doping based on the contact dielectric substrate.[37] Importantly, it is necessary to point out that the new method can in principle induce a much higher carrier density at $\sim10^{13}$ cm^{-2} with an improved sample quality.[38] Moreover, the doping capability of this heterostructure may be further enhanced by replacing CIPS with some other 2D ferroelectric materials, such as α-In$_2$Se$_3$.[39] For this reason, this system may provide a possible way to realize physics in the high density limit, in which the many-body effect is dominated.

CONCLUSIONS

In summary, we have presented a 2D ferroelectric heterostructure device that is capable of continuously tuning the optical property of monolayer MoSe$_2$ with electrical nonvolatility. Such a retentive electrostatic gating effect originates from the OOP electric polarization in 2D ferroelectric CIPS. To our knowledge, the clear charge carrier recoil effect for both electron and hole trions is observed in a single device for the first time. Our results provide a route to develop novel functional nanoelectronic devices with van der Waals materials as well as a method to explore emergent physical properties with 2D ferroelectrics.

METHODS

Sample Preparation and Device Fabrication. Bulk single-crystal CIPS in this study was purchased from HQ Graphene, Inc. Bulk single-crystal MoSe$_2$ was synthesized by the chemical vapor transportation method. Mixed molybdenum (99.99%) and selenium powder (99.99%) with a 1:3 atomic ratio were sealed in a quartz tube under vacuum conditions ($\sim10^{-5}$ Torr). The vacuum-sealed quartz tube was then placed in a two-zone electrical tube furnace. The growth temperature was set to be around 1080 °C with a slow heating process for a time duration of 48 h. The high-temperature growth was kept for 1 week. After the growth, it was then slowly cooled down to room temperature in 1 week. Ultrathin CIPS and monolayer MoSe$_2$ were obtained by mechanical exfoliation on polydimethylsiloxane (PDMS, Gel-Pak, WF-60-X4). Few-layer CIPS and monolayer MoSe$_2$

were prepared on PDMS by the mechanical exfoliation method. Using the all-dry transfer method,[40] few-layer CIPS was transferred onto the surface of the pre-prepared Au electrode. Monolayer $MoSe_2$ was stacked on the CIPS thin layer in the same way. By post-stacking $MoSe_2$, two electrodes were bridged, allowing the DC or pulsed voltage to be applied to the heterostructure devices. The device electrodes were fabricated via the standard photoetching method with the deposition of 5 nm titanium and 25 nm gold via an e-beam evaporator.

Electrical Polarization Process. The polarizing pulse voltage was applied through a source/measure unit (Keysight Technologies B2912). The pulse duration period is 0.2 s with a width of 0.001 s. Each voltage pulse is repeated for 30 periods. The DC mode tests on Device 4# were performed with the same instrument.

PFM Measurement. PFM measurements were performed with AIST-SmartSPM by using a Pt−Ir-coated conducting Si tip under ambient conditions. The conductive substrates used in this study were prepared through sputtering a 30 nm thick gold film onto a Si substrate with 90 nm SiO_2 on the top. The PFM configuration for ferroelectric domain writing is depicted in Figure 3a. By sweeping the sample surface by applying a −5.6 V tip bias, we flipped the polarization direction to be upward in the center with a square region (2 μm × 2 μm).

Optical Measurements. The PL measurement was performed via a Princeton Instruments spectrometer (IsoPlane SCT 320) with a continuous wave solid-state 532 nm laser. With a home-made microscope setup, the laser was focused to a spot with a diameter of ∼2 μm. The laser intensity was kept at below 10 μW to prevent light doping or exciton generation from high-power excitation in all the measurements. When obtaining the PL spectrum, all the devices were placed in a cryogenic chamber (Montana Instruments), which is capable of tuning the sample temperature from 7 to 300 K.

ASSOCIATED CONTENT

Supporting Information

The Supporting Information is available free of charge at https://pubs.acs.org/doi/10.1021/acsami.1c03067.

Additional characterization results including PFM, PL, and FET measurements and schematic of the electron recoil effect (PDF)

AUTHOR INFORMATION

Corresponding Authors

Ming Gong − *CAS Key Laboratory of Quantum Information, University of Science and Technology of China, Hefei 230026, People's Republic of China; Synergetic Innovation Center of Quantum Information and Quantum Physics, University of Science and Technology of China, Hefei, Anhui 230026, China*; Email: gongm@ustc.edu.cn

Hualing Zeng − *International Center for Quantum Design of Functional Materials (ICQD), Hefei National Laboratory for Physical Science at the Microscale, and Synergetic Innovation Center of Quantum Information and Quantum Physics, University of Science and Technology of China, Hefei, Anhui 230026, China; Key Laboratory of Strongly-Coupled Quantum Matter Physics, Department of Physics, Chinese Academy of Sciences, University of Science and Technology of China, Hefei, Anhui 230026, China*; orcid.org/0000-0001-5869-9553; Email: hlzeng@ustc.edu.cn

Authors

Xiaoyu Mao − *International Center for Quantum Design of Functional Materials (ICQD), Hefei National Laboratory for Physical Science at the Microscale, and Synergetic Innovation Center of Quantum Information and Quantum Physics, University of Science and Technology of China, Hefei, Anhui 230026, China; Key Laboratory of Strongly-Coupled Quantum Matter Physics, Department of Physics, Chinese Academy of Sciences, University of Science and Technology of China, Hefei, Anhui 230026, China*; orcid.org/0000-0003-0849-2436

Jun Fu − *International Center for Quantum Design of Functional Materials (ICQD), Hefei National Laboratory for Physical Science at the Microscale, and Synergetic Innovation Center of Quantum Information and Quantum Physics, University of Science and Technology of China, Hefei, Anhui 230026, China; Key Laboratory of Strongly-Coupled Quantum Matter Physics, Department of Physics, Chinese Academy of Sciences, University of Science and Technology of China, Hefei, Anhui 230026, China*

Chen Chen − *International Center for Quantum Design of Functional Materials (ICQD), Hefei National Laboratory for Physical Science at the Microscale, and Synergetic Innovation Center of Quantum Information and Quantum Physics, University of Science and Technology of China, Hefei, Anhui 230026, China; Key Laboratory of Strongly-Coupled Quantum Matter Physics, Department of Physics, Chinese Academy of Sciences, University of Science and Technology of China, Hefei, Anhui 230026, China*

Yue Li − *International Center for Quantum Design of Functional Materials (ICQD), Hefei National Laboratory for Physical Science at the Microscale, and Synergetic Innovation Center of Quantum Information and Quantum Physics, University of Science and Technology of China, Hefei, Anhui 230026, China; Key Laboratory of Strongly-Coupled Quantum Matter Physics, Department of Physics, Chinese Academy of Sciences, University of Science and Technology of China, Hefei, Anhui 230026, China*

Heng Liu − *International Center for Quantum Design of Functional Materials (ICQD), Hefei National Laboratory for Physical Science at the Microscale, and Synergetic Innovation Center of Quantum Information and Quantum Physics, University of Science and Technology of China, Hefei, Anhui 230026, China; Key Laboratory of Strongly-Coupled Quantum Matter Physics, Department of Physics, Chinese Academy of Sciences, University of Science and Technology of China, Hefei, Anhui 230026, China*

Complete contact information is available at: https://pubs.acs.org/10.1021/acsami.1c03067

Author Contributions

X.M., J.F., and C.C. contributed equally to this work. H.Z. conceived the idea and supervised the research. X.M., Y.L., and J.F. prepared the samples. X.M., J.F., and C.C. fabricated the devices and carried out the transport, PFM, and Raman spectroscopy measurements of the 2D ferroelectric device. X.M., J.F., M.G., and H.Z. analyzed the data and wrote the article, and all authors commented on the manuscript.

Notes

The authors declare no competing financial interest.

ACKNOWLEDGMENTS

This work was supported by the National Key Research and Development Program of China (grant nos. 2017YFA0205004 and 2018YFA0306600), the National Natural Science Foundation of China (grant no. 11674295), the Fundamental Research Funds for the Central Universities (grant nos. WK3510000013 and WK2030020032), the Anhui Initiative in Quantum Information Technologies (grant no. AHY170000), and the China Government Youth 1000-Plan Talent Program. This work was partially carried out at the USTC Center for Micro and Nanoscale Research and Fabrication.

REFERENCES

(1) Gong, Y.; Liu, Z.; Lupini, A. R.; Shi, G.; Lin, J.; Najmaei, S.; Lin, Z.; Elías, A. L.; Berkdemir, A.; You, G.; Terrones, H.; Terrones, M.; Vajtai, R.; Pantelides, S. T.; Pennycook, S. J.; Lou, J.; Zhou, W.; Ajayan, P. M. Band Gap Engineering and Layer-by-Layer Mapping of Selenium-Doped Molybdenum Disulfide. *Nano Lett.* **2014**, *14*, 442−449.

(2) Ugeda, M. M.; Bradley, A. J.; Shi, S.-F.; da Jornada, F. H.; Zhang, Y.; Qiu, D. Y.; Ruan, W.; Mo, S.-K.; Hussain, Z.; Shen, Z.-X.; Wang, F.; Louie, S. G.; Crommie, M. F. Giant Bandgap Renormalization and Excitonic Effects in a Monolayer Transition Metal Dichalcogenide Semiconductor. *Nat. Mater.* **2014**, *13*, 1091−1095.

(3) Raja, A.; Chaves, A.; Yu, J.; Arefe, G.; Hill, H. M.; Rigosi, A. F.; Berkelbach, T. C.; Nagler, P.; Schüller, C.; Korn, T.; Nuckolls, C.; Hone, J.; Brus, L. E.; Heinz, T. F.; Reichman, D. R.; Chernikov, A. Coulomb Engineering of the Bandgap and Excitons in Two-Dimensional Materials. *Nat. Commun.* **2017**, *8*, 15251.

(4) Zhang, X. X.; You, Y.; Zhao, S. Y.; Heinz, T. F. Experimental Evidence for Dark Excitons in Monolayer WSe$_2$. *Phys. Rev. Lett.* **2015**, *115*, 257403.

(5) Mak, K. F.; He, K.; Lee, C.; Lee, G. H.; Hone, J.; Heinz, T. F.; Shan, J. Tightly Bound Trions in Monolayer MoS$_2$. *Nat. Mater.* **2013**, *12*, 207−211.

(6) Wang, Z.; Rhodes, D. A.; Watanabe, K.; Taniguchi, T.; Hone, J. C.; Shan, J.; Mak, K. F. Evidence of High-Temperature Exciton Condensation in Two-Dimensional Atomic Double Layers. *Nature* **2019**, *574*, 76−80.

(7) You, Y.; Zhang, X.-X.; Berkelbach, T. C.; Hybertsen, M. S.; Reichman, D. R.; Heinz, T. F. Observation of Biexcitons in Monolayer WSe$_2$. *Nat. Phys.* **2015**, *11*, 477−481.

(8) Li, Y.; Liu, W.; Ren, H.; Feng, Q.; Yan, J.; Zhong, W.; Xin, X.; Xu, H.; Liu, Y. Enhanced Carrier−Exciton Interactions in Monolayer MoS$_2$ under Applied Voltages. *ACS Appl. Mater. Interfaces* **2020**, *12*, 18870−18876.

(9) Zeng, H.; Dai, J.; Yao, W.; Xiao, D.; Cui, X. Valley Polarization in MoS$_2$ Monolayers by Optical Pumping. *Nat. Nanotechnol.* **2012**, *7*, 490−493.

(10) Mak, K. F.; He, K.; Shan, J.; Heinz, T. F. Control of Valley Polarization in Monolayer MoS$_2$ by Optical Helicity. *Nat. Nanotechnol.* **2012**, *7*, 494−498.

(11) Zhu, B.; Zeng, H.; Dai, J.; Gong, Z.; Cui, X. Anomalously Robust Valley Polarization and Valley Coherence in Bilayer WS$_2$. *Proc. Natl. Acad. Sci. U.S.A.* **2014**, *111*, 11606−11611.

(12) Mak, K. F.; Lee, C.; Hone, J.; Shan, J.; Heinz, T. F. Atomically Thin MoS$_2$: A New Direct-Gap Semiconductor. *Phys. Rev. Lett.* **2010**, *105*, 136805.

(13) Splendiani, A.; Sun, L.; Zhang, Y.; Li, T.; Kim, J.; Chim, C.-Y.; Galli, G.; Wang, F. Emerging Photoluminescence in Monolayer MoS$_2$. *Nano Lett.* **2010**, *10*, 1271−1275.

(14) Zhang, Y.; Chang, T.-R.; Zhou, B.; Cui, Y.-T.; Yan, H.; Liu, Z.; Schmitt, F.; Lee, J.; Moore, R.; Chen, Y.; Lin, H.; Jeng, H.-T.; Mo, S.-K.; Hussain, Z.; Bansil, A.; Shen, Z.-X. Direct Observation of the Transition from Indirect to Direct Bandgap in Atomically Thin Epitaxial MoSe$_2$. *Nat. Nanotechnol.* **2014**, *9*, 111−115.

(15) Chernikov, A.; Berkelbach, T. C.; Hill, H. M.; Rigosi, A.; Li, Y.; Aslan, O. B.; Reichman, D. R.; Hybertsen, M. S.; Heinz, T. F. Exciton Binding Energy and Nonhydrogenic Rydberg Series in Monolayer WS$_2$. *Phys. Rev. Lett.* **2014**, *113*, 076802.

(16) Mouri, S.; Miyauchi, Y.; Matsuda, K. Tunable Photoluminescence of Monolayer MoS$_2$ via Chemical Doping. *Nano Lett.* **2013**, *13*, 5944−5948.

(17) Sercombe, D.; Schwarz, S.; Del Pozo-Zamudio, O.; Liu, F.; Robinson, B. J.; Chekhovich, E. A.; Kolosov, O.; Tartakovskii, A. I. Optical Investigation of the Natural Electron Doping in Thin MoS$_2$ Films Deposited on Dielectric Substrates. *Sci. Rep.* **2013**, *3*, 3489.

(18) Nan, H.; Wang, Z.; Wang, W.; Liang, Z.; Lu, Y.; Chen, Q.; He, D.; Tan, P.; Miao, F.; Wang, X.; Wang, J.; Ni, Z. Strong Photoluminescence Enhancement of MoS$_2$ through Defect Engineering and Oxygen Bonding. *ACS Nano* **2014**, *8*, 5738−5745.

(19) Ross, J. S.; Wu, S.; Yu, H.; Ghimire, N. J.; Jones, A. M.; Aivazian, G.; Yan, J.; Mandrus, D. G.; Xiao, D.; Yao, W.; Xu, X. Electrical Control of Neutral and Charged Excitons in a Monolayer Semiconductor. *Nat. Commun.* **2013**, *4*, 1474.

(20) Ross, J. S.; Klement, P.; Jones, A. M.; Ghimire, N. J.; Yan, J.; Mandrus, D. G.; Taniguchi, T.; Watanabe, K.; Kitamura, K.; Yao, W.; Cobden, D. H.; Xu, X. Electrically Tunable Excitonic Light-Emitting Diodes Based on Monolayer WSe$_2$ P-N Junctions. *Nat. Nanotechnol.* **2014**, *9*, 268−272.

(21) Shang, J.; Shen, X.; Cong, C.; Peimyoo, N.; Cao, B.; Eginligil, M.; Yu, T. Observation of Excitonic Fine Structure in a 2D Transition-Metal Dichalcogenide Semiconductor. *ACS Nano* **2015**, *9*, 647−655.

(22) Ko, C. Reconfigurable Local Photoluminescence of Atomically-Thin Semiconductors via Ferroelectric-Assisted Effects. *Nanomaterials* **2019**, *9*, 1620.

(23) Li, C. H.; McCreary, K. M.; Jonker, B. T. Spatial Control of Photoluminescence at Room Temperature by Ferroelectric Domains in Monolayer WS$_2$/PZT Hybrid Structures. *ACS Omega* **2016**, *1*, 1075−1080.

(24) Nguyen, A.; Sharma, P.; Scott, T.; Preciado, E.; Klee, V.; Sun, D.; Lu, I.-H.; Barroso, D.; Kim, S.; Shur, V. Y.; Akhmatkhanov, A. R.; Gruverman, A.; Bartels, L.; Dowben, P. A. Toward Ferroelectric Control of Monolayer MoS$_2$. *Nano Lett.* **2015**, *15*, 3364−3369.

(25) Wen, B.; Zhu, Y.; Yudistira, D.; Boes, A.; Zhang, L.; Yidirim, T.; Liu, B.; Yan, H.; Sun, X.; Zhou, Y.; Xue, Y.; Zhang, Y.; Fu, L.; Mitchell, A.; Zhang, H.; Lu, Y. Ferroelectric-Driven Exciton and Trion Modulation in Monolayer Molybdenum and Tungsten Diselenides. *ACS Nano* **2019**, *13*, 5335−5343.

(26) Lv, L.; Zhuge, F.; Xie, F.; Xiong, X.; Zhang, Q.; Zhang, N.; Huang, Y.; Zhai, T. Reconfigurable Two-Dimensional Optoelectronic Devices Enabled by Local Ferroelectric Polarization. *Nat. Commun.* **2019**, *10*, 3331.

(27) Li, D.; Huang, X.; Xiao, Z.; Chen, H.; Zhang, L.; Hao, Y.; Song, J.; Shao, D. F.; Tsymbal, E. Y.; Lu, Y.; Hong, X. Polar Coupling Enabled Nonlinear Optical Filtering at MoS$_2$/Ferroelectric Heterointerfaces. *Nat. Commun.* **2020**, *11*, 1422.

(28) Xiao, Z.; Song, J.; Ferry, D. K.; Ducharme, S.; Hong, X. Ferroelectric-Domain-Patterning-Controlled Schottky Junction State in Monolayer MoS$_2$. *Phys. Rev. Lett.* **2017**, *118*, 236801.

(29) Bennett, J. W.; Grinberg, I.; Rappe, A. M. New Highly Polar Semiconductor Ferroelectrics through d^8 Cation-O Vacancy Substitution into PbTiO$_3$: A Theoretical Study. *J. Am. Chem. Soc.* **2008**, *130*, 17409−17412.

(30) Lu, H.; Liu, X.; Burton, J. D.; Bark, C.-W.; Wang, Y.; Zhang, Y.; Kim, D. J.; Stamm, A.; Lukashev, P.; Felker, D. A.; Folkman, C. M.; Gao, P.; Rzchowski, M. S.; Pan, X. Q.; Eom, C.-B.; Tsymbal, E. Y.; Gruverman, A. Enhancement of Ferroelectric Polarization Stability by Interface Engineering. *Adv. Mater.* **2012**, *24*, 1209−1216.

(31) Stengel, M.; Vanderbilt, D.; Spaldin, N. A. Enhancement of Ferroelectricity at Metal-Oxide Interfaces. *Nat. Mater.* **2009**, *8*, 392−397.

(32) Liu, F.; You, L.; Seyler, K. L.; Li, X.; Yu, P.; Lin, J.; Wang, X.; Zhou, J.; Wang, H.; He, H.; Pantelides, S. T.; Zhou, W.; Sharma, P.; Xu, X.; Ajayan, P. M.; Wang, J.; Liu, Z. Room-Temperature Ferroelectricity in CuInP$_2$S$_6$ Ultrathin Flakes. *Nat. Commun.* **2016**, *7*, 12357.

(33) Christopher, J. W.; Goldberg, B. B.; Swan, A. K. Long Tailed Trions in Monolayer MoS$_2$: Temperature Dependent Asymmetry and Resulting Red-Shift of Trion Photoluminescence Spectra. *Sci. Rep.* **2017**, *7*, 14062.

(34) Yan, J.; Zhang, Y.; Kim, P.; Pinczuk, A. Electric Field Effect Tuning of Electron-Phonon Coupling in Graphene. *Phys. Rev. Lett.* **2007**, *98*, 166802.

(35) Das, A.; Pisana, S.; Chakraborty, B.; Piscanec, S.; Saha, S. K.; Waghmare, U. V.; Novoselov, K. S.; Krishnamurthy, H. R.; Geim, A. K.; Ferrari, A. C.; Sood, A. K. Monitoring Dopants by Raman Scattering in an Electrochemically Top-Gated Graphene Transistor. *Nat. Nanotechnol.* **2008**, *3*, 210−215.

(36) Stampfer, C.; Molitor, F.; Graf, D.; Ensslin, K.; Jungen, A.; Hierold, C.; Wirtz, L. Raman Imaging of Doping Domains in Graphene on SiO_2. *Appl. Phys. Lett.* **2007**, *91*, 241907.

(37) Ueno, K.; Shimotani, H.; Yuan, H.; Ye, J.; Kawasaki, M.; Iwasa, Y. Field-Induced Superconductivity in Electric Double Layer Transistors. *J. Phys. Soc. Jpn.* **2014**, *83*, 032001.

(38) Wu, J.; Chen, H.-Y.; Yang, N.; Cao, J.; Yan, X.; Liu, F.; Sun, Q.; Ling, X.; Guo, J.; Wang, H. High Tunnelling Electroresistance in a Ferroelectric Van Der Waals Heterojunction Via Giant Barrier Height Modulation. *Nat. Electron.* **2020**, *3*, 466−472.

(39) Zhou, Y.; Wu, D.; Zhu, Y.; Cho, Y.; He, Q.; Yang, X.; Herrera, K.; Chu, Z.; Han, Y.; Downer, M. C.; Peng, H.; Lai, K. Out-of-Plane Piezoelectricity and Ferroelectricity in Layered Alpha-In_2Se_3 Nanoflakes. *Nano Lett.* **2017**, *17*, 5508−5513.

(40) Castellanos-Gomez, A.; Buscema, M.; Molenaar, R.; Singh, V.; Janssen, L.; van der Zant, H. S. J.; Steele, G. A. Deterministic Transfer of Two-Dimensional Materials by All-Dry Viscoelastic Stamping. *2D Mater* **2014**, *1*, 011002.